

# The pre-wetting transition at antiphase boundaries: an atomistic modeling study of Ni<sub>3</sub>Al

Chandler Amiss Becker · Yuri Mishin ·  
William J. Boettinger

Received: 7 July 2007 / Accepted: 21 November 2007 / Published online: 6 March 2008  
© Springer Science+Business Media, LLC 2008

**Abstract** Using an embedded-atom model for Ni–Al alloys, we have examined interfacial properties of the Ni/Ni<sub>3</sub>Al system, concentrating on properties of the antiphase boundaries. These interfaces between domains of the  $\gamma'$  phase can undergo a pre-wetting transition as the region of the antiphase boundaries disorders and then transforms into a metastable  $\gamma$  phase. In order to understand more about this transition, we have performed detailed thermodynamic, compositional, and structural analyses of this system using semi-grand canonical Monte-Carlo simulations, with particular interest in composition profiles and segregation. We will discuss our studies in the context of previous treatments of these interfaces.

## Introduction

Ni<sub>3</sub>Al is a technologically important intermetallic compound that remains strongly ordered up to the melting point at 1,658 K. It crystallizes in the FCC-based L1<sub>2</sub> structure whose cubic unit cell contains Al atoms in the corners and Ni atoms at the centers of the faces. This structure can be represented as four interpenetrating sublattices, one of which is occupied by Al and three others by Ni. Ni<sub>3</sub>Al demonstrates unusual mechanical properties, particularly an anomalous increase of yield stress with temperature up to about 900–1,000 K [1]. The chemical composition of

Ni<sub>3</sub>Al can deviate from the exact stoichiometry, giving rise to a wide  $\gamma'$  phase on the Ni–Al phase diagram [2]. On the Ni-rich side, the  $\gamma'$  phase is separated by a two-phase region from a  $\gamma$  phase, which represents a disordered solid solution based on FCC Ni.

Solidification of the  $\gamma'$  phase results in L1<sub>2</sub>-ordered domains separated from each other by antiphase boundaries (APBs). While the FCC lattice is continuous across each APB, the preferential occupations of the sublattices are shifted relative to each other. Solidification is not the only mechanism of APB formation. Precipitation of small  $\gamma'$  particles from a supersaturated  $\gamma$  phase produces a highly disperse structure responsible for the high strength of precipitation-hardened Ni-base superalloys [3, 4]. As the  $\gamma'$  particles grow, they eventually begin to impinge on each other and, if their orderings are different, form APBs. The atomic structure and thermodynamic stability of the APBs can affect the  $\gamma'$  coarsening kinetics and thus the evolution of mechanical properties of the alloy. In addition, lattice dislocations that penetrate into the  $\gamma'$  phase during plastic deformation dissociate into superpartial dislocations separated by APBs [5–9]. These APBs affect the dislocation mobility and thus mechanical strength of the alloy. It is, therefore, important to understand how temperature, bulk chemical composition and other factors affect the local chemical composition, long-range order and the excess free energy of APBs in the  $\gamma'$  phase.

An interesting effect associated with  $\gamma'$  APBs is the possibility of their transformation into a thin disordered layer with properties similar to those of the bulk  $\gamma$  phase. Indeed, in the classical sharp-interface model, if the APB free energy  $\gamma_{\text{APB}}$  is greater than twice the free energy of the  $\gamma/\gamma'$  interface, the APB can split into two  $\gamma/\gamma'$  interfaces bounding a region of  $\gamma$ . This transformation can be viewed as a wetting of the APB with the  $\gamma$  phase. This, in turn, can

---

C. A. Becker (✉) · W. J. Boettinger  
Metallurgy Division, National Institute of Standards  
and Technology, Gaithersburg, MD 20899, USA  
e-mail: chandler.becker@nist.gov

Y. Mishin  
Physics Department, George Mason University, Fairfax,  
VA 22030, USA

inhibit the  $\gamma'$  coalescence and coarsening kinetics and can have impact on structural stability of the alloy. Even if the temperature and bulk composition are in the single-phase  $\gamma'$  region on the phase diagram, a  $\gamma$ -like layer could still form at APBs. This would correspond to a pre-wetting interfacial transition at APBs and is the subject of the present paper.

Wetting and pre-wetting transitions at APBs have been studied by different computational methods. Kikuchi and Cahn [10] applied the cluster variation method (CVM) with multiatom interactions to model APBs in Cu–Au alloys. Finel et al. [11] studied (100) APBs in  $L1_2$  alloys by CVM and Monte-Carlo simulations, finding that the wetting layer width increased as the critical temperature was approached according to  $\log(T_c - T)$ , where  $T_c$  was the critical temperature. Sluiter and Kawazoe [12] studied (111) APBs in  $Ni_3Al$  using CVM combined with first-principles calculations. Ni enrichment and partial disorder at APBs in  $Ni_3Al$  were also observed by Monte-Carlo simulations with an embedded-atom potential [13]. Braun et al. [14] developed a multiple-order-parameter phase-field model to capture the anisotropy of the APB free energy and to study APB wetting transitions in FCC alloys. Phase-field simulations specifically for the Ni–Al system [15] have demonstrated that the APB wetting can play an important role in stabilizing the rafted microstructure of  $\gamma + \gamma'$  alloys by discouraging the coarsening of  $\gamma'$  particles. The experimental finding of a lower barrier to  $\gamma$  precipitate coalescence in the  $\gamma'$  matrix than for  $\gamma'$  precipitates in the  $\gamma$  matrix [16] supports the role of APBs in the resistance to coalescence.

In this work, we apply atomistic Monte-Carlo simulations with a realistic atomic interaction model to examine (111) APBs in the  $\gamma'$  phase. The quantities of primary interest are the APB width, the chemical composition and order parameters in the APB region, and the Gibbsian excess of Ni. The formation of a  $\gamma$ -like layer at the APB during the pre-wetting is verified by the local chemical composition and order parameters approaching those of the bulk  $\gamma$  phase.

Following [14], we characterize the ordered state of the  $\gamma$  and  $\gamma'$  phases by four parameters,

$$c = \frac{1}{4}(\rho_1 + \rho_2 + \rho_3 + \rho_4), \quad (1)$$

$$\eta_1 = \frac{1}{4}(\rho_1 + \rho_2 - \rho_3 - \rho_4), \quad (2)$$

$$\eta_2 = \frac{1}{4}(\rho_1 - \rho_2 + \rho_3 - \rho_4), \quad (3)$$

$$\eta_3 = \frac{1}{4}(\rho_1 - \rho_2 - \rho_3 + \rho_4). \quad (4)$$

Here  $\rho_i$  is the atomic fraction of Al on sublattice  $i$  ( $0 \leq \rho_i \leq 1$ ),  $c$  represents the overall chemical composition of

the phase averaged over the four sublattices, and  $\eta_i$  characterize the long-range order. (Note that our notations differ from those in [14] in the use of  $c$  and  $\eta_i$  instead of  $W$ ,  $X$ ,  $Y$ , and  $Z$ .) In the  $\gamma$  phase we have  $\eta_1 = \eta_2 = \eta_3 = 0$  due to the absence of long-range order. In perfectly ordered stoichiometric  $Ni_3Al$ , we have  $c = |\eta_1| = |\eta_2| = |\eta_3| = 0.25$ . This relation can be satisfied with one of the sublattice concentrations  $\rho_i$  being equal to unity and the three others equal to zero. These four choices of the Al sublattice give rise to the four possible types of ordered domains.

## Methodology

### Simulations of bulk phases

Atomic interactions in the Ni–Al system were modeled by the embedded-atom method (EAM) potential developed in [13]. The potential reproduces a number of properties of the  $\gamma$  and  $\gamma'$  phases, as well as the  $\gamma/\gamma'$  equilibrium lines on the phase diagram in reasonable agreement with experiment [2].

We will begin by discussing simulations of homogeneous  $\gamma$  and  $\gamma'$  phases. The goal of these simulations was to obtain a relation between the imposed chemical potential difference between Al and Ni,  $\Delta\mu = \mu_{Al} - \mu_{Ni}$ , and the chemical compositions of the phases. In this work, the chemical composition is always measured by the atomic fraction  $c$  of Al atoms defined by Eq. (1). A relation between  $\Delta\mu$  and  $c$  is needed for the APB simulations discussed later.

In order to compute thermodynamic properties of the phases, we used Monte-Carlo (MC) simulations in the semi-grand canonical ensemble, in which  $\Delta\mu$ , temperature  $T$ , pressure  $P = 0$ , and the total number of atoms  $N$  are fixed, while the volume and the chemical composition are allowed to vary to achieve thermodynamic equilibrium [17, 18]. In order to maintain zero pressure, the three dimensions of a rectangular simulation block are allowed to change independently. Trial moves of the Metropolis algorithm that we used include random changes of atom type (Ni to Al or vice versa), random atomic displacements, and random dimension changes (expansion or contraction) along the  $\hat{x}$ ,  $\hat{y}$  and  $\hat{z}$  directions parallel to the edges of the block. Most of the simulation runs were performed in a block containing  $N = 4704$  atoms with periodic boundary conditions in all three directions. In order to verify convergence with respect to the model size, simulations for  $\Delta\mu = 0.5$  eV were repeated using a larger block with  $N = 10,800$  atoms. The results were found to be statistically indistinguishable from those for the  $N = 4,704$  block.

Two types of initial configurations were used for each  $\Delta\mu$ : either pure Ni or perfectly stoichiometric Ni<sub>3</sub>Al. After the block was brought to thermodynamic equilibrium, its equilibrium chemical composition and lattice parameter were determined by averaging over at least  $2 \times 10^3$  MC steps (trial moves) per atom. All simulations reported in this work were performed at  $T = 700$  K; a study of the temperature effect is deferred to a separate publication. At this temperature, the bulk chemical compositions of the phases and the corresponding lattice parameters were computed for a range of  $\Delta\mu$  values with a small step.

### Simulations of antiphase boundaries

Simulations of APBs in the  $\gamma'$  phase were performed in a periodic simulation block containing initially stoichiometric Ni<sub>3</sub>Al with crystallographic directions  $[\bar{1}10]$ ,  $[111]$  and  $[\bar{1}\bar{1}2]$  aligned parallel to the block edges  $\hat{x}$ ,  $\hat{y}$  and  $\hat{z}$ , respectively. Two different block sizes were used:  $12 \times 60 \times 24$  ( $N = 11,520$ ) and  $12 \times 90 \times 24$  ( $N = 17,280$ ). Both blocks represent a stack of 60 (respectively, 90) (111) planes normal to the  $\hat{y}$ -direction. The larger block was preferable for more diffuse APBs arising near the  $\gamma'$  solvus line and was used for  $\Delta\mu \geq 0.40$  eV in order to have a region of bulk-like Ni<sub>3</sub>Al and minimize APB interactions. A copy of the initial block was saved and later used as a reference configuration for data processing (see below). An initial (111) APB was created at the center of the block by applying a  $[a/\sqrt{2}, 0, 0]$  translation parallel to  $\hat{x}$  to all atoms on one side of a chosen (111) plane. This also produced a second APB, parallel to the first one, at the outer edges of the block due to the periodic boundary conditions.

The MC runs were again performed in the semi-grand canonical ensemble at  $T = 700$  K and  $P = 0$ . A series of imposed  $\Delta\mu$  values was applied in order to examine the APB at different bulk compositions  $c_{\gamma'}$  on the Ni-rich side of the stoichiometry. Each simulation was first run for 1,000 MC steps per atom to equilibrate the block. For statistical averaging of equilibrium properties, the equilibration run was followed by a production run consisting of at least  $1.23 \times 10^4$  MC steps. During the production run, snapshots of atomic configurations were recorded every 150 MC steps. This interval was chosen to be longer than the characteristic correlation period of the system variables, such as the total energy and composition, as recorded at each MC step.

### Analysis methods

For each snapshot saved during the production runs of the simulations, the atoms were mapped onto the closest

reference sites. The reference configuration represented the same simulation block, but with perfect Ni<sub>3</sub>Al stoichiometry and without an APB. Prior to the mapping, the reference configuration was expanded by the thermal expansion factor known from the bulk simulations with the same  $c_{\gamma'}$ . Note that this mapping procedure assigns each atom to a particular sublattice of the reference crystal. The chemical compositions  $\rho_i$  of the sublattice sites were then averaged over each (111) layer, producing sublattice composition profiles  $\rho_i(y)$  ( $y$  is distance along  $\hat{y}$ ). They were used to compute the average composition profile  $c(y)$  and the order parameter profiles  $\eta_i(y)$  from Eqs. 1–4.

Due to the translation vector used to generate the APB, sublattice 1 of one  $\gamma'$  domain and sublattice 2 of the adjacent  $\gamma'$  domain are initially filled with pure Al, whereas sublattices 3 and 4 are filled with pure Ni on both sides of the APB. Thus, at stoichiometry and 0 K, the functions  $\rho_1(y)$  and  $\rho_2(y)$  make jumps between 0 and 1 across the APB, whereas  $\rho_3(y)$  and  $\rho_4(y)$  remain identically zero. At finite temperatures and/or away from the bulk stoichiometry, the bulk values of  $\rho_i$  deviate from 1 and 0, and the jumps of  $\rho_1$  and  $\rho_2$  smear out over several atomic planes. This smearing produces minima of  $c(y)$  and  $\eta_1(y)$  at the center of the APB region. At the same time, the profiles  $\rho_3(y)$  and  $\rho_4(y)$  develop maxima at the center of the APB, reflecting the partial loss of order. Note that by crystal symmetry,  $\rho_3$  and  $\rho_4$  must be statistically equivalent at every point, thus  $\eta_2$  and  $\eta_3$  must also be identical [14]. This was indeed verified by the MC simulations. We will, therefore, exclude the profiles  $\rho_4(y)$  and  $\eta_3(y)$  from further discussion.

In order to quantify these effects, we first used the sublattice composition profiles  $\rho_1$  and  $\rho_2$  to locate the APBs in individual snapshots. This was done by locating the positions  $y_1$ th and  $y_2$ th along  $\hat{y}$  where  $\rho$  crossed a threshold value chosen to be  $0.7 \times (\rho^{\max} - \rho^{\min})$ . The APB thickness  $H$  was then defined by

$$H = y_2\text{th} - y_1\text{th}. \quad (5)$$

Alternatively, we could fit the site profiles  $\rho_1(y)$  and  $\rho_2(y)$  across the central APB with hyperbolic tangent functions:

$$\rho_i = h - a \times \tanh((d - y)/b) \quad (6)$$

where  $h$ ,  $a$ ,  $d$ , and  $b$  are fitting parameters. Using either Eqs. 5 or 6, similar trends in width were observed with changing  $c_{\gamma'}$  except that the second criterion produced slightly wider boundaries. However, the functional form in Eq. 6 does not allow for a double tangent shape predicted for  $\gamma/\gamma'$  coexistence, so the first method was selected for single snapshots.

For the averaged snapshots, we fit profiles  $c(y)$  and  $\eta_1(y)$  deduced from the MC simulations by a combination of hyperbolic tangents,

$$c(y) = A_c - B_c \left[ \tanh\left(\frac{y - d_{c1}}{\delta_c}\right) - \tanh\left(\frac{y - d_{c2}}{\delta_c}\right) \right], \quad (7)$$

$$\eta_1(y) = A - B \left[ \tanh\left(\frac{y - d_1}{\delta}\right) - \tanh\left(\frac{y - d_2}{\delta}\right) \right], \quad (8)$$

where  $A$ ,  $A_c$ ,  $B$ ,  $B_c$ ,  $d_1$ ,  $d_2$ ,  $d_{c1}$ ,  $d_{c2}$ ,  $\delta$  and  $\delta_c$  are fitting parameters. These functions are appealing for two reasons. First, they give the correct shape of the profiles, i.e., a symmetric minimum with horizontal asymptotes on either side. Second, tanh is expected to describe the composition and order-parameter profiles across an isolated  $\gamma/\gamma'$  interface [19]. Thus, if the APB dissociates in two  $\gamma/\gamma'$  interfaces (wetting with  $\gamma$ ), Eqs. 7 and 8 give accurate descriptions of the APB profiles. However, this double tangent form was not fit well by individual snapshots due to the large number of fitting parameters and statistical noise. It was only used to fit profiles generated by averaging snapshots, since the noise was reduced.

The fact that  $c(y)$  attains a minimum indicates that the APB region is enriched in Ni. The degree of this enrichment (Ni segregation) was characterized by two quantities. The first one is the minimum value of  $c(y)$ ,  $c^{\min} = \min(c(y))$ , which was averaged over all snapshots of the MC run. The second quantity is the Gibbsian excess  $\Gamma_{Ni}$ , which is usually defined as the number of excess atoms (relative to the bulk) per unit interface area. In this work, however, we chose to express  $\Gamma_{Ni}$  as the effective number of Ni monolayers (ML) using the equation

$$\Gamma_{Ni} = \frac{1}{2N_m} (N_{APB}^{Ni} - N_{bulk}^{Ni}).$$

Here  $N_m = 192$  is the number of lattice sites in each (111) layer of the simulation block,  $N_{APB}^{Ni}$  and  $N_{bulk}^{Ni}$  are the numbers of Ni atoms in the block computed with and without the APB and averaged over all MC steps of the production run. The factor 2 in this equation takes into account that there are effectively two APBs in the block. The ML units are more appropriate for the analysis of APB transformations, since the total number of atoms in each (111) layer does not vary with the bulk composition whereas the APB area does.

The degree of local disorder at the APB is characterized by the depth of the minimum of the  $\eta_1(y)$  profile,  $\eta_1^{\min} = \min(\eta_1(y))$ . This quantity was determined for each profile and averaged over all snapshots.

For the quantities  $c^{\min}$ ,  $\eta_1^{\min}$ ,  $H$  and  $\Gamma_{Ni}$ , the standard error was computed from the scatter of the values obtained from individual snapshots. The error bars in the plots shown below represent twice these standard deviations.

There can be two ways to average composition and order-parameter profiles over multiple snapshots. One is to shift each individual profile so that the minimum would be attained at  $y = 0$ . This “recentering” of the profiles can be

achieved by the transformation  $y \rightarrow y - d_m$ , where  $d_m = (y_{2th} + y_{1th})/2$  is the center of the profile estimated using the fitted values of  $y_{1th}$  and  $y_{2th}$ . The average profile is then obtained by averaging the concentrations and order parameters within individual (111) layers. Alternatively, the profiles can be averaged without recentering. Since the APB tends to wander around its average position during the simulations, the neglect of the recentering leads to somewhat broader profiles and somewhat higher  $c^{\min}$  and  $\eta_1^{\min}$  values. This was verified by computing the quantities  $H$ ,  $c^{\min}$ , and  $\eta_1^{\min}$  from profiles averaged both ways. In the results presented here, we used the recentered profiles to minimize APB broadening associated with its motion.

## Results and discussion

### Thermodynamics of bulk phases

Figure 1 shows the bulk compositions of the  $\gamma$  and  $\gamma'$  phases obtained as functions of the imposed  $\Delta\mu$ . For  $\Delta\mu$  values below  $\approx 0.50$  eV, the equilibration of the simulation block always resulted in homogeneous  $\gamma'$  phase regardless of whether the initial configuration was pure Ni or Ni<sub>3</sub>Al. In some of the runs starting with Ni, we were able to observe nucleation and growth of  $\gamma'$  domains. The domains impinged on each other and produced APBs, which later migrated away from the simulation block and finally produced a single-domain  $\gamma'$  state. Likewise, simulations with  $\Delta\mu > 0.54$  eV always gave homogeneous  $\gamma$  phase regardless of the initial configuration. In these simulations, the identities of the phases were determined from their chemical compositions and order parameters  $\eta_i$ .

A hysteresis was found between  $\Delta\mu \approx 0.50$  eV and 0.54 eV. In this  $\Delta\mu$  range, simulations starting from pure Ni gave homogeneous  $\gamma$  phase that did not undergo any further transformation during the simulations (at least  $2 \times 10^3$  MC steps per atom). On the other hand, simulations starting with Ni<sub>3</sub>Al resulted in homogeneous  $\gamma'$  phase that did not transform into  $\gamma$  during the same number of MC steps.

The observation of the hysteresis is consistent with the known fact that the  $\gamma - \gamma'$  phase transformation is first order. Unfortunately, the MC method does not give direct access to free energy and thus does not permit direct calculations of the two-phase equilibrium point. Although the thermodynamic integration and other methods could be applied to this end [18], this was not pursued in this article. Instead, taking advantage of the rather narrow hysteresis loop, the  $\gamma - \gamma'$  equilibrium at 700 K was estimated by the midpoint of the loop,  $\Delta\mu = 0.52$  eV. The corresponding equilibrium compositions of the phases are  $c_\gamma^{eq} = 0.140$  and  $c_{\gamma'}^{eq} = 0.233$ . Both numbers are in good agreement with

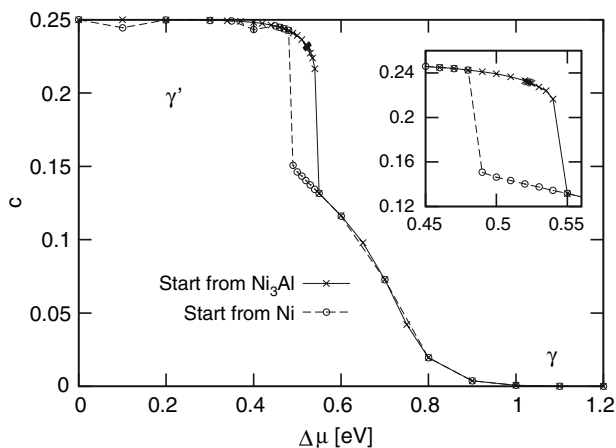


**Fig. 1** At a fixed temperature of 700 K, the Al concentration decreases in both the  $\gamma$  and  $\gamma'$  phases with increasing values of the imposed chemical potential difference  $\Delta\mu$ . A hysteresis region exists around  $\Delta\mu \approx 0.52$  eV, in which the phase state depends on the initial configuration of the simulations. The lines connect the data points

previous calculations using thermodynamic integration ( $c_{\gamma}^{eq} = 0.137$  and  $c_{\gamma'}^{eq} = 0.233$ , respectively) [13]. Accordingly, the points in Fig. 1 corresponding to the  $\gamma$  phase at  $\Delta\mu = 0.50$ – $0.52$  eV and  $\gamma'$  phase at  $\Delta\mu = 0.52$ – $0.54$  eV represent thermodynamically metastable states of the phases.

Interfacial properties

When the bulk composition  $c_{\gamma'}$  is close to the stoichiometry, the concentration and order-parameter profiles are sharp but still smeared over a few atomic layers, see example in Fig. 2 ( $c_{\gamma'} = 0.246$  corresponds to  $\Delta\mu = 0.44$  eV). The insets in this figure reveal a very small peak of  $\rho_3$  and minima of  $c$  and  $\eta_1$  at the center of the APB region. Note that the profiles  $c(y)$  and  $\eta_1(y)$  are very close to each other, which is consistent with Eqs. 1–4 for small values of  $\rho_3$  and  $\rho_4$ . Most of the Al atoms remain on sublattices 1 and 2 and switch between them across the APB.

As  $c_{\gamma'}$  decreases and approaches the two-phase equilibrium concentration  $c_{\gamma'}^{eq}$ , the APB profiles broaden and develop shapes indicative of the formation of a  $\gamma$ -like layer. This is illustrated in Fig. 3. The profiles have a minimum at the center of the APB and tend to a constant value away from the APB which equals the bulk composition  $c_{\gamma'}$ . For reference, the plot indicates the equilibrium solvus compositions  $c_{\gamma}^{eq} = 0.140$  and  $c_{\gamma'}^{eq} = 0.233$ . The APB profiles are given for  $\Delta\mu$  in the range of  $0 \leq \Delta\mu \leq 0.525$  eV. It also shows a profile obtained at  $\Delta\mu = 0.54$  eV after the initial  $\gamma'$  phase has completely transformed to  $\gamma$  during the simulation. As expected, this profile is flat and corresponds to a composition slightly below  $c_{\gamma}^{eq}$ . Observe that, as  $c_{\gamma'}$

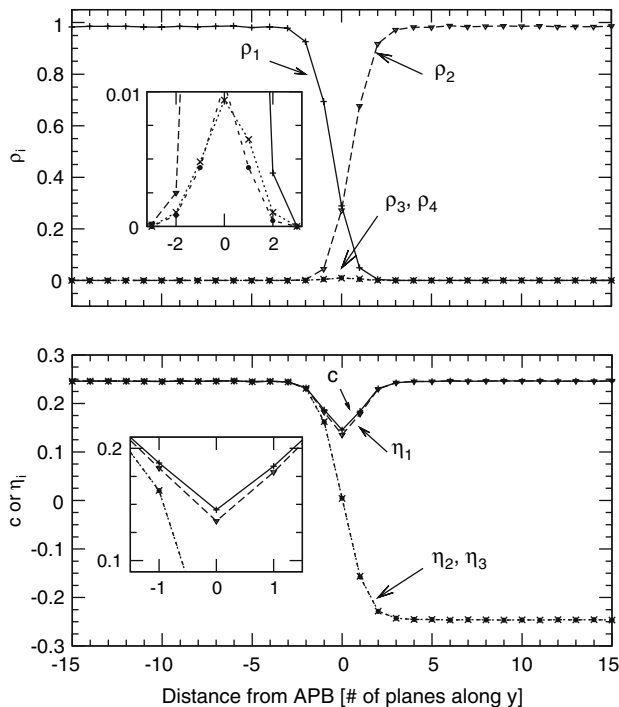


**Fig. 2** Upper: Site compositions for  $c_{\gamma'} = 0.246$  on each of the four  $\text{Ni}_3\text{Al}$  sublattices, with an inset of the APB region. Lower: Composition  $c(y)$  and order parameters  $\eta_1(y)$ ,  $\eta_2(y)$ , and  $\eta_3(y)$  with the behavior of  $c(y)$  and  $\eta_1(y)$  highlighted in the APB region. In both panels, the APB is in the center, while the outer edges represent  $\gamma'$  regions. Lines connecting the points are meant as guides

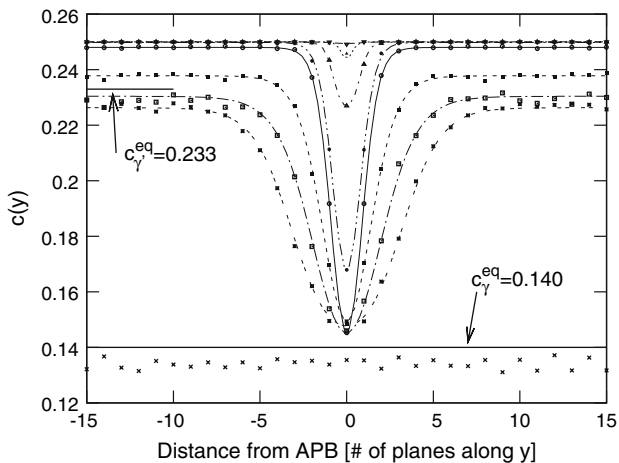


**Fig. 3** Composition profiles  $c(y)$  across the APB for different values of the bulk  $\gamma'$  composition  $c_{\gamma'}$ . The widths and depths of the profiles increase with decreasing  $c_{\gamma'}$ , eventually transforming the APB into a layer of the  $\gamma$  phase. The upper curves correspond to  $0 \leq \Delta\mu \leq 0.525$  eV, while the bottom set of points was obtained for  $\Delta\mu = 0.54$  eV after transformation to the  $\gamma$  phase. The APB profiles are averaged over multiple snapshots using the centering procedure described in the text. Lines on APB profiles represent profile fits by Eq. 7

decreases, the concentration minimum becomes wider while  $c^{\min}$  rapidly decreases until it reaches a level close to  $c_{\gamma}^{eq}$ . After that,  $c^{\min}$  remains nearly constant, while the

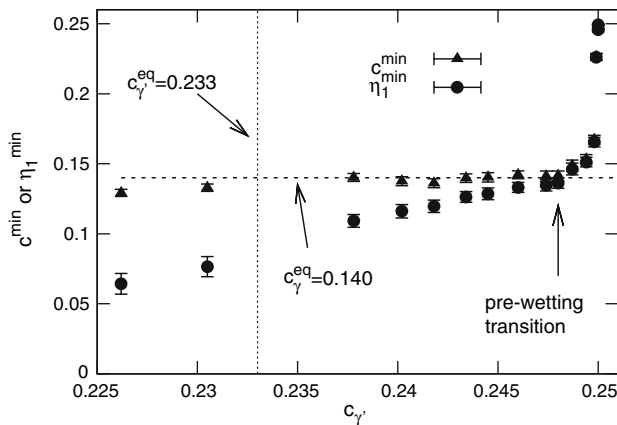


**Fig. 4** APB composition ( $c^{\min}$ ) and order parameter  $\eta_1^{\min}$  as determined by averaging the minimum planar values for each snapshot.  $c^{\min}$  and  $\eta_1^{\min}$  decrease with decreasing bulk  $c_{\gamma'}$  until values approach those of  $\gamma$  ( $c_{\gamma'}^{\text{eq}} = 0.140$  and  $\eta_1^{\min} = 0$ )

profile continues to broaden. The lines in Fig. 3 were fits of the averaged profiles to Eq. 7.

The two lowest curves in Fig. 3 represent metastable states of the bulk  $\gamma'$  phase, for which  $c_{\gamma'} < c_{\gamma'}^{\text{eq}}$ . These profiles were obtained during the initial part of the simulations, when the simulation block remained in the  $\gamma'$  phase with an APB.

Figure 4 shows a plot of  $c^{\min}$  and  $\eta_1^{\min}$  as functions of the bulk composition  $c_{\gamma'}$ . Near the bulk stoichiometry we have  $c^{\min} \approx \eta_1^{\min} \approx 0.25$ . As  $c_{\gamma'}$  slightly departs from the stoichiometry, both  $c^{\min}$  and  $\eta_1^{\min}$  rapidly drop but remain nearly identical. As the off-stoichiometry increases further, the two quantities diverge:  $c^{\min}$  levels out at approximately  $c_{\gamma'}^{\text{eq}}$ , whereas  $\eta_1^{\min}$  continues to decrease.

This effect is revealed more clearly in Fig. 5, where we plot  $\eta_1^{\min}$  versus  $c^{\min}$ . As long as  $c_{\gamma'}$  is above 0.248, the points follow a straight line with a unit slope, indicating that  $c^{\min} \approx \eta_1^{\min}$ . According to Eqs. 1–4, this relation means that the deficit of Al atoms is accommodated almost exclusively by sublattices 1 and 2, whereas sublattices 3 and 4 remain filled with almost pure Ni ( $\rho_3 = \rho_4 \rightarrow 0$ ). At  $c_{\gamma'} \approx 0.248$ , the slope increases dramatically:  $\eta_1^{\min}$  suddenly begins to decrease while  $c^{\min}$  remains almost constant and close to  $c_{\gamma'}^{\text{eq}} = 0.140$ . At this point Al atoms begin to penetrate into sublattices 3 and 4 within the APB region, shifting the balance towards more uniform distribution between the four sublattices. This point can be taken as a pre-wetting transition in the APB, at which it becomes similar to a layer of the  $\gamma$  phase. The pre-wet concentration range thus corresponds to  $c_{\gamma'}$  between approximately  $c_{\gamma'}^{\text{eq}} = 0.233$  and  $c_{\gamma'} \approx 0.248$ .

The fact that  $\eta_1^{\min}$  never actually reaches zero indicates that the APB retains some degree of order even when the bulk  $\gamma'$  phase reaches thermodynamic equilibrium with  $\gamma$ . Furthermore, the two lowest points in Fig. 5 represent the

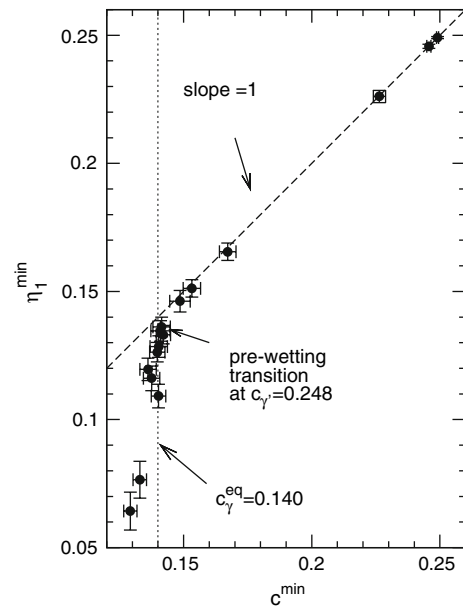


**Fig. 5** Order parameters  $\eta_1^{\min}$  versus  $c^{\min}$  are almost equal until  $c^{\min}$  reaches  $c_{\gamma'}^{\text{eq}}$ , at which point they diverge. That divergence indicates the pre-wetting transition near  $c_{\gamma'} = 0.248$ . The dashed line indicates  $\eta_1^{\min} = c^{\min}$

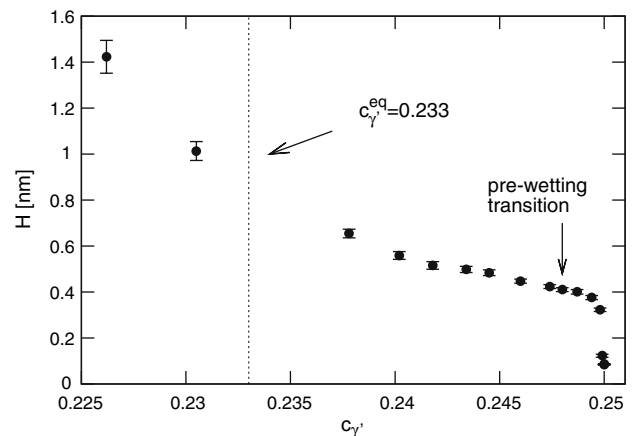


**Fig. 6** The APBs become wider as  $c_{\gamma'}$  decreases, ranging from a very narrow APB near  $\text{Ni}_3\text{Al}$  stoichiometry to an APB width of approximately 1.0 nm for  $c_{\gamma'}$  near the  $\gamma'/(\gamma + \gamma')$  solvus

APB in the metastable  $\gamma'$  phase. Although  $\eta_1^{\min}$  continues to decrease, it is still above zero.

The APB width  $H$  is plotted in Fig. 6 as a function of  $c_{\gamma'}$ . After the initial very rapid increase near the bulk stoichiometry, the growth of  $H$  slows down as it reaches the pre-wetting point. Further departure from the bulk off-stoichiometry produces a new increase of  $H$ , corresponding to a rapid growth of the  $\gamma$  layer. Importantly, the APB width remains finite when the bulk composition reaches the solvus line, and even when the bulk  $\gamma'$  becomes metastable. Although the APB becomes increasingly more diffuse, its

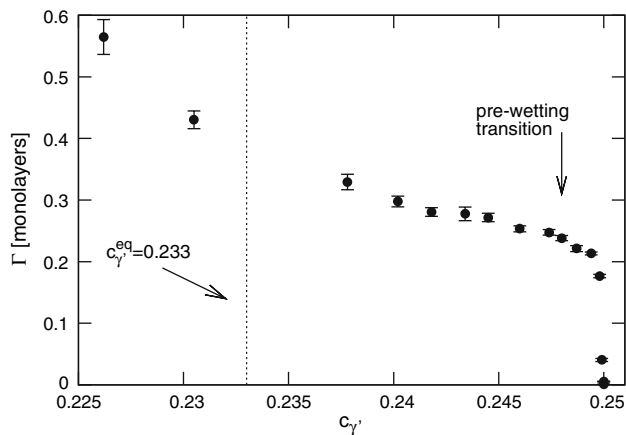


**Fig. 7** Adsorption (excess Ni at the APB) displays a similar trend as the APB widths, increasing with decreasing  $c_{\gamma'}$  in the  $\gamma'$  phase

thickness is never found to exceed 2 nm. This is consistent with the existence of the residual order in the APB (non-zero  $\eta_1^{\min}$  values): the adjacent ordered domains impose some degree of ordering on the APB region as long as the latter is relatively narrow.

The behavior of the Gibbsian adsorption  $\Gamma_{Ni}$  (Fig. 7) is consistent with what one would expect from the rough estimate

$$\Gamma_{Ni} \propto (c_{\gamma'} - c^{\min})H.$$

Indeed, the initial growth and then saturation of  $\Gamma_{Ni}$  with the deviation from the stoichiometry are due to the concurrent decrease in  $c^{\min}$  (higher Ni concentration in the APB) and increase in  $H$  (wider APB), cf. Figs. 5 and 6. After the pre-wetting transition, the factor  $(c_{\gamma'} - c^{\min})$  becomes almost constant, while  $\Gamma_{Ni}$  continues to increase due to the APB broadening.

## Conclusions

We have applied semi-grand canonical Monte-Carlo simulations to examine the behavior of the (111) APB the  $\gamma'$  phase of the Ni–Al system. The APB thickness, local chemical composition and the local order parameters have been calculated as functions of the bulk composition at a fixed temperature of 700 K. The distinct feature of this work in comparison with previous studies [10–12] is that the atomic interactions are modeled accurately enough to reproduce the relevant part of the experimental Ni–Al phase diagram, and that all configurational effects and the atomic vibrations are included without any approximations.

The APB region is found to be always enriched in Ni and less ordered than the bulk  $\gamma'$  phase. As the Al bulk concentration  $c_{\gamma'}$  decreases, the APB composition approaches the composition of the  $\gamma$  phase,  $c_{\gamma}^{eq}$ , while the local

long-range order parameter becomes small (although not zero). This verifies that the APB turns into a thin disordered layer whose properties are similar to those of the bulk  $\gamma$  phase. This transformation, called the APB pre-wetting, is predicted to occur at  $c_{\gamma'} \approx 0.248$  at 700 K, above  $c_{\gamma'}^{eq} = 0.233$ . At this point the local order parameter in the APB region begins to drop rapidly with decreasing  $c_{\gamma'}$ , whereas the APB composition remains nearly constant and close to  $c_{\gamma}^{eq}$ .

An important finding is that the (111) APB thickness  $H$  remains finite when  $c_{\gamma'}$  reaches the solvus composition, and even when the bulk  $\gamma'$  phase becomes metastable. This is contrary to other studies reporting a continuous increase of  $H$  and its divergence near the solvus for (100) APBs [11]. The finite-thickness APB pre-wet with  $\gamma$  observed in our work at the solvus line clearly represents only one solution of the problem, the other solution being a replacement of the APB by a macroscopically thick  $\gamma$  layer (complete wetting). When the bulk  $\gamma'$  phase becomes metastable with respect to  $\gamma$ , the pre-wet APB becomes metastable with respect to the completely wet APB, whose free energy can be reduced continuously by making it thicker. The fact that we were able to observe this metastable state of the APB points to the existence of a free-energy barrier separating it from the complete wetting; overcoming this barrier takes a certain number of MC steps, during which we were able to compute the APB profiles.

This represents the first part of a broader study to examine the properties of these APBs using combined atomistic and phase-field approaches.

**Acknowledgements** C. B. would like to thank the NIST-NRC postdoctoral research associateship program for research support and J. E. Guyer for helpful discussions. Y. M. acknowledges the support of the U. S. Department of Energy, Office of Basic Energy Sciences.

## References

1. Pope DP (1996) Physical metallurgy, vol 3, chap 24. Elsevier/North-Holland, Amsterdam, p 207
2. Massalski TB (eds) (1986) Binary alloy phase diagrams. ASM, Materials Park, OH
3. Sims CT, Stoloff NS, Hagel WC (eds) (1987) Superalloys II—high-temperature materials for aerospace and industrial applications. Wiley, New York
4. Pollock TM, Kissinger RD, Bowman RR, Green KA, McLean M, Olson SL, Schirra JJ (eds) (2000) Superalloys. TMS, Warrendale
5. Yoo MH, Daw MS, Baskes MI (1989) In: Vitek V, Srolovitz DJ (eds) Atomistic simulation of materials: beyond pair potentials. Plenum Press, New York, 1989, p 401
6. Pasianot R, Farkas D, Savino EJ (1991) J Phys III 1:997
7. Vitek V, Ackland GJ, Cserti J (1991) Phase stability and design. In: Giamei P, Pope DP (eds) MRS Symp Proc, vol 186, pp 237–251
8. Vitek V, Pope DP, Bassani JL (1996) In: Nabarro FRN, Duesbery MS (eds) Dislocations in solids, vol 10, chap 51. Elsevier/North-Holland, Amsterdam, p 136
9. Wen M, Li S (1998) Acta Mater 46:4351

10. Kikuchi R, Cahn JW (1979) Theory of interphase and antiphase boundaries in F.C.C. alloys. *Acta Metall* 7:1337
11. Finel A, Mazauric V, Ducastelle F (1990) Theoretical study of antiphase boundaries in fcc alloys. *Phys Rev Lett* 65:1016
12. Sluiter M, Kawazoe Y (1998) A study of the thermodynamics of segregation and partial order at (111) antiphase boundaries in Ni<sub>3</sub>Al. *Philos Mag A* 78:1353
13. Mishin Y (2004) Atomistic modeling of the  $\gamma$  and  $\gamma'$ -phases of the Ni–Al system. *Acta Mater* 52:1451
14. Braun RJ, Cahn JW, McFadden GB, Wheeler AA (1997) Anisotropy of interfaces in an ordered alloy: a multiple-order-parameter model. *Phil Trans R Soc Lond A* 355:1787
15. Wang Y, Banerjee D, Su CC, Khachatryan AG (1998) Field kinetic model and computer simulation of precipitation of L1<sub>2</sub> ordered intermetallics from F.C.C. solid solution. *Acta Mater* 46:2983
16. Ma Y, Ardell AJ (2005) Coarsening of  $\gamma$  (Ni–Al solid solution) precipitates in a  $\gamma'$  (Ni<sub>3</sub>Al) matrix; a striking contrast in behavior from normal  $\gamma/\gamma'$  alloys. *Scripta Mater* 52:1335
17. Foiles SM, Daw MS (1987) Application of the embedded atom method to Ni<sub>3</sub>Al. *J Mater Res* 2:5
18. Frenkel D, Smit B (2002) *Understanding molecular simulation: from algorithms to applications*, 2nd edn. Academic Press, San Diego
19. Cahn JW, Hilliard JE (1959) Free energy of a nonuniform system. 3. nucleation in a 2-component incompressible fluid. *J Chem Phys* 31:688